Ocean Engineering 60 (2013) 28–38

Contents lists available at SciVerse ScienceDirect

Ocean Engineering

journal homepage: www.elsevier.com/locate/oceaneng

Flow characteristics and tip vortex formation around a NACA 0018 foil with an endplate

Ok-Sok Gim*, Gyoung-Woo Lee

Department of Naval Architecture & Ocean Engineering, Mokpo National Maritime University, Mokpo 534-729, South Korea

ARTICLE INFO

Article history:
Received 1 May 2012
Accepted 1 December 2012
Available online 26 January 2013

Keywords:
NACA 0018
Reynolds shear stress
Endplate
Tip vortex
Flow characteristics
Particle Image Velocimetry (PIV)

ABSTRACT

Tip vortex structure around a NACA 0018 foil with and without an endplate is studied using PIV method in a circulating water channel. The Reynolds number based on the chord length (100 mm) is $Re=2.5\times10^4$. The analysis also includes varying angles of attack $\alpha=10^\circ$ and $\alpha=20^\circ$. Velocity profiles are obtained from 1C (chord length) to 3C, measured from the trailing edge. Sectional velocity profiles are also obtained and compared both foils at the same angles of attack. Vortex formation is changed near the end-span section due to the prevention of roll-up phenomenon. The endplate also decreases Reynolds shear stress in the wake region. It can be judged that the flow formation around the foil is affected by the endplate untill the mid-span.

1. Introduction

Control surfaces are used on a wide range of marine vehicles as rudders, stabilizers and pitch damping foils. The fundamental concept of a movable device to steer a ship has been in use since ships were conceived. The purpose of the devices, or rudders, is either to maintain the ship on a particular course or direction, or to enable it to manoeuvre. It may be composed of a single movable surface or the combination of fixed and movable devices. An extensive amount of researches and investigations into ship rudders and control surfaces has been carried out for years, including wide ranging investigations by the authors into rudder–propeller interaction (Ahn and Kim, 2003; Paik et al., 2010; Lam et al., 2011). The hydrodynamic forces and moment induced by propellers and rudders are formulated based on the flow fields around the propellers and rudders Kobayashi and Ishbashi (1993).

The practical use of special rudders has increased with the advantage of stability, course keeping ability, navigational safety, maneuverability and work efficiency. Maneuverability has been received a great deal of attention both concerning navigation safety and the prediction of ship-steering characteristics, especially at the preliminary design stage. Maneuvering characteristics have not been clarified due to the complicated hydrodynamic forces at the stern form, propellers, rudders and skegs. These forces and moment are generated as a result of rudder rotations and attack angles then determine the maneuvering characteristics of marine vehicles. These impart turning or yawing motions to the vehicles.

Lee et al. (2008) reported that the development of a high-lift rudder is needed because of the maneuvering of low speed full ships. The vessels have difficult to obtain enough side forces from a common rudder. The design of high-lift rudder should be considered with the interactions between hull, propellers and rudders. Tang and Dowell (2006) carried out an experiment on flow control devices based on an oscillating foil with small trailing edge strips. The device can significantly increase the maximum dynamic lift and the stall angles of attack. Gurney flap can move the separation position forward on the lower surface. Farsimadan and Dehghan (2010) conducted an experimental study on the near-wake of a NACA 0012 placed upstream of a 90° bend section. They confirmed that the freestream velocity alters the boundary layer development on the foil and that the flow angle has more effect on the boundary layer development on the upper surface of the foil. Yu et al. (2005) and Cory et al. (1998) carried out a numerical simulation on the effect of Gurney flap over a foil. Gurney flaps increase the foil lift coefficient with only a slight increase in drag coefficient. The separation point of the foil with a Gurney flap rests farther aft at moderate angles of attack than that of a clean foil. They insisted a significant increase in lift-to-drag ratio relatively at low angles of attack. Weier and Gerbeth (2004) insisted that Lorentz forces could be used to influence the flow of conducting fluids. They applied time periodic Lorentz forces to the control of the suction side flow on a NACA 0015 hydrofoil within the range of $10^4 \le Re \le 10^5$. The Lorentz force allows for a great flexibility in providing the time dependency of the forcing.

* Tel.: +82 10 2614 3001.
E-mail address: domingo@mmu.ac.kr (O.-S. Gim).

0029-8018/$ - see front matter © 2012 Elsevier Ltd. All rights reserved.
http://dx.doi.org/10.1016/j.oceaneng.2012.12.009

They offer a potential for further energetic optimization of the flow control by unsteady Lorentz forces.

Seo et al. (2007) reported that a considerable improvement in performance of a fin stabilizer is achieved with adoption of the tail blades. Wang et al. (2009) also studied a drag-based active fin stabilizer used in zero-speed conditions based on the reaction force from the fluid.

Daichin and Zhao (2007) investigated on the near wake flow of an airfoil above the free surface in a wind-wave tunnel at $Re=3.5\times10^3$ using PIV system. The lift force and pressure drag acting on the airfoil increased as the airfoil was getting closer to the free surface.

Grant et al. (2006) carried out an experimental investigation to measure the total lift and induced drag of NACA 0015. In compared with previous researches using Pitot pressure techniques and CFD, they proved that PTV is a viable tool in obtaining quantitative flow field characteristics rapidly. PIV time-averaged data allowed a more exact comparison with CFD and traditional data collection methods.

On the historical technical notes of Pass (1940), the endplate effect of the horizontal tail increases the effective aspect ratio of a single vertical tail by about 50%. Other technical notes for Carter (1961), the endplate prevent the flow exiting through the wing tip instead of the small gap at the trailing edge and increase the ground effect exerting on the wing surface. It noted that the endplate effect of preventing the stagnated air on lower surface from flowing out around the wing tips and produced a substantial improvement in lift-drag ratio. Park and Lee (2008) and Park et al. (2008) numerically studied on the effect of an endplate at various angles of attack for a wings-in-ground craft. They found that the endplate prevented the high-pressure air from escaping out of the lower surface and so reduced the influence of the tip vortex and further augmented the lift and lift-drag ratio. The endplate also reduced the deviation of the static height stability with respect to angles and heights. The purpose of the present paper is to investigate the influence of an endplate on the flow around a foil at $Re=2.5\times10^4$. Two-dimensional flow characteristics around NACA 0018 with and without an endplate was investigated. The experiment was carried out with 10 and 20 angles of attack to obtain the flow information around the foil using two-frame grey-level cross-correlation PIV method.

2. Experimental setup and conditions

The rudder model used for this study consists of NACA 0018 with and without a plate in a flow. Experiments were conducted in a circulating free surface water channel on a case-by-case basis. The coordinate system adapted through the whole experiments is shown in Fig. 1. It is to measure two dimensional flow characteristics of the rudder. The angles of attack (α) are varied 10°, 20° respectively. The channel has a section of 1000 mm (L) $\times$ 300 mm (W) $\times$ 300 mm (H) which is made from 15 mm-thick transparency Plexiglas sheet. The water as a working fluid used in this experiment was kept at a constant value of 25 ± 1 °C, fresh water. The water pump is driven by an electric motor with a variable speed controller. The flow is driven by the effect of gravity under atmospheric conditions in room temperature. The model is installed in the middle of the water channel which has a distance h=300 mm between the free surface and the bottom of channel. The experimental configuration used in this study consists of a flow imposed around a rudder at a Reynolds number ($Re=2.5\times10^4$) based on the chord length 100 mm.

The l overview of the circulating water channel with the model installed is shown in Fig. 3. The distribution of u-components is more complicated near the bottom than the free surface of the channel. That is the reason why the Reynolds number should be

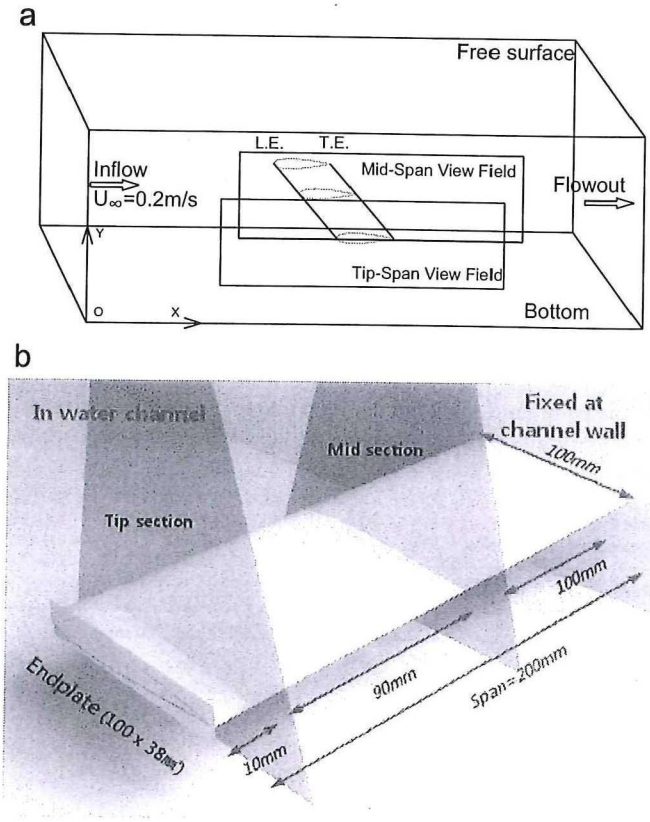

Fig. 1. Schematic diagram of model setup and coordinate system. (a) Circulating water channel and coordinate system and (b) Physical model setup, location of mid-span section and tip-span section.

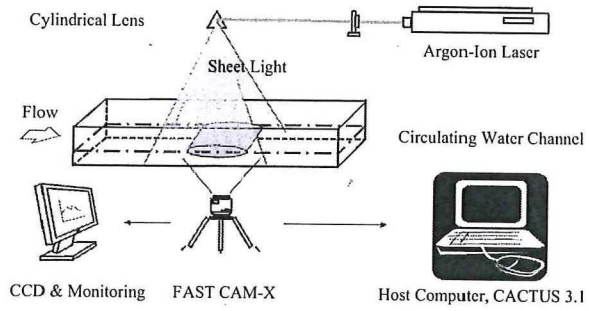

Fig. 2. Schematic arrangement of PIV system.

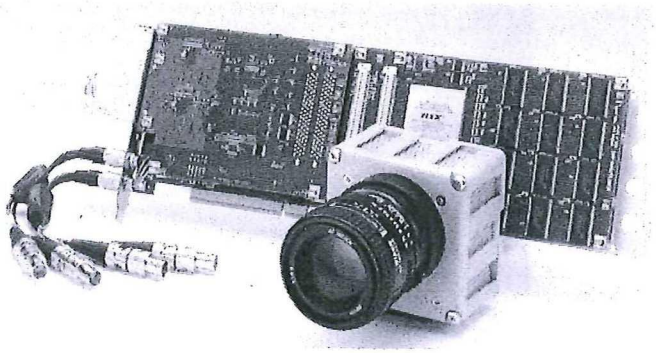

Fig. 3. High-speed camera and image grabber.

$Re=2.5\times10^4$ in this study. The model is an endplate foil consists of NACA 0018, 100 mm in chord length. The dimensions of the endplate which is attached at the span end of the foil is a rectangular plate,

100 mm (L) × 360 mm (W) in Fig. 1(b). The field of view for mid-span section is 100 mm from the wall side. The field of view for tip-span section is 190 mm from the wall side. The model is installed in the water channel as a cantilever that consists of 200 mm-span long. One side of the model is fixed at the wall and the other side of the model is free as shown in Fig. 1. The axis of rotation to change angles of attack is 1/3 of chord length from the leading edge. The model is made of acrylic acid resin, so that laser light propagates easily through the model. Fig. 2 shows the schematic views of PIV system equipment. It is a powerful optical method used to measure velocities and related properties in flow fluids. PIV method has been applied to a wide range of flow problems, varying from the flow over an object in a wind tunnel to vortex formation in heat valves. The algorithms based on two-frame grey-level cross-correlation can be implemented in a matter of time. In this study, 1600 frames are calculated to obtain the time-mean flow information. The fluid is seeded with particles, which for the purposes of PIV, are generally assumed to follow the flow dynamics. It is the motion of these seeding particles that is used to calculate velocity information. Measurements were conducted using PIV system that consists of an optical LED laser, high-speed digital camera (FASTCAM-X 1280PCI) and an image grabber as shown in Fig. 3. It is a powerful optical method of fluid visualization that is used to obtain velocity field and related properties in flow fluids. The digital camera provides the resolution of 1280 × 1024 pixel image at frame rates to 500 fps (frames per second), and at reduced resolutions up to 16,000 fps. A powerful LED arrayed laser (wavelength 532 nm) with an optical arrangement is used to convert the laser output light to a light sheet using a cylindrical lens. The laser acts as a photographic flash for the digital camera. Particles in the fluid scatter the light. The camera can detect this scattered light. The fluid is seeded with tracer particles, which are assumed to faithfully follow the flow dynamics. The polyamide particles with a mean diameter of 150 μm and the density of 1.02 g/cm^3 are used as the seeding particles. Flow visualization was performed for the bare foil without an end plate by a high-resolution digital camera. The whole experimental conditions are described in details in Table 1.

Table 1
Experimental conditions.

Item	Specification
Light source	LED Lasers (Wave length 532 nm–500 mW)
Sheet light	Cylindrical lens (Width=2 mm)
Working fluid	Fresh water (25 ± 1 °C)
Time resolution	125 fps
Grid (X × Y)	120 × 80
Particle	PVC (ρ: 1.02 Φ:150)
Dimension (NACA0018)	Chord length: 100 mm Span length: 200 mm
Algorithm	Two-frame grey-level cross correlation (CACTUS v.3.1)

3. Results and discussion

Fig. 4 shows the flow visualization around NACA 0018 foil at attack angles α=10°, 15° and 20° without an endplate at mid-span section. It shows flow formation for each angle of attack, which is taken photos being exposed during 0.5 s by a camera. It includes instantaneous visual flow information with the location of flow separation and vortex formation clearly visible in the flow field. Although the turbulent flow around a two-dimensional foil is

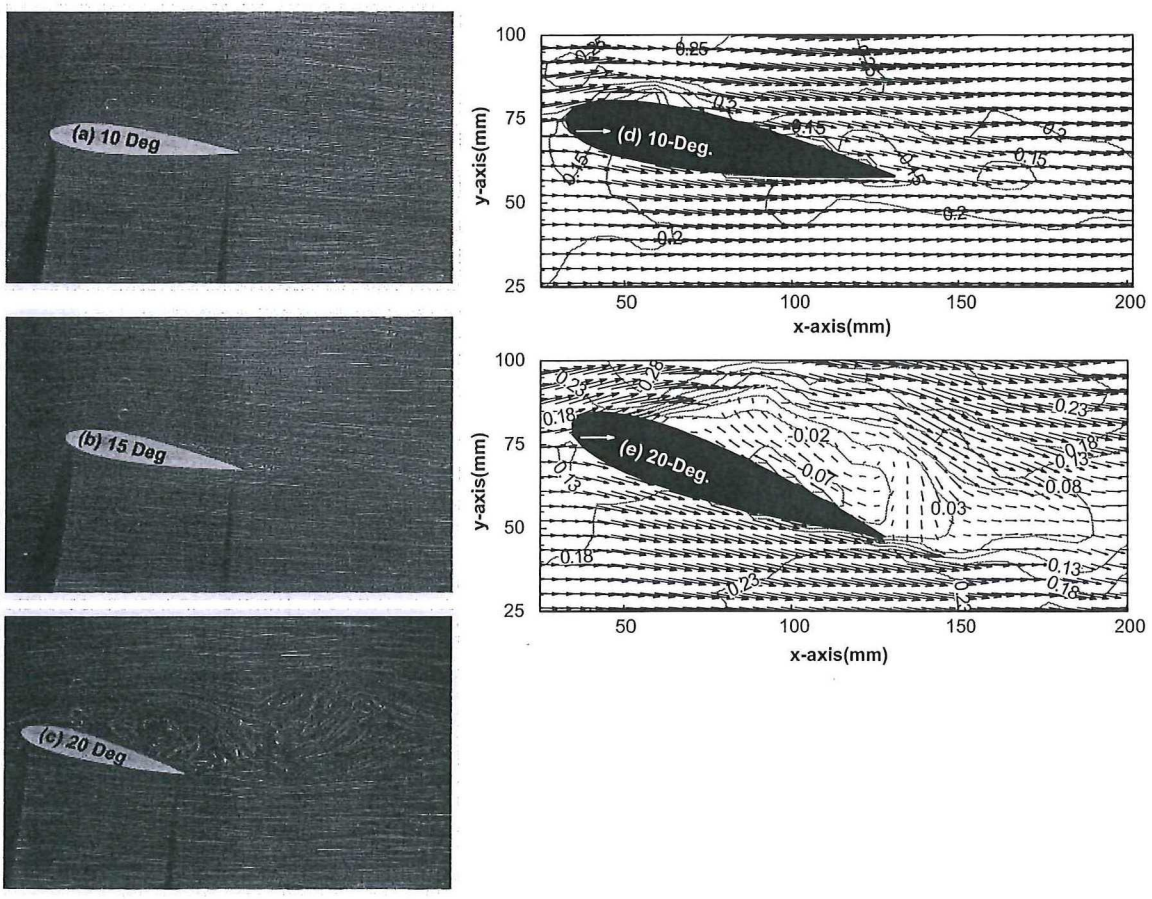

Fig. 4. Flow visualization and velocity field around NACA 0018 foil.

inherently three-dimensional, the two-dimensional flow field gives us better understanding for the development of flow separation and flow patterns. In Fig. 4(a) at $\alpha=10^{\circ}$, the flow separation does not occur at any point, which the flow runs through the foil surface smoothly. It is formed laminar flow and thin boundary layer based on the velocity field of Fig. 4(d) at $\alpha=10^{\circ}$. If the flow follows the foil surface, it will lead to friction due to fluid viscosity. The flow velocities near the foil surface are decreased due to the friction. Generally, there are two factors to affect the increase of lift force. One is the inflow velocity and the other is the variance of attack angles. Therefore, the density and inflow velocity magnitude remains constant in this case. Another factor is the variance of attack angles.

With an increase of attack angles $\alpha=15^{\circ}$ in Fig. 4(b), the flow separation starts near the trailing edge of the foil surface. The flow leaves at the trailing edge with turbulent flow. It will start decrease lift force because of not the flow follows foil surface. The velocities on the foil surface decrease due to the pressure difference between the inside and outside of the boundary layer because of the flow separation.

With further increase in attack angles to $\alpha=20^{\circ}$, Fig. 4(c), the flow is separated completely from the foil surface of the leading edge. The separating shear layer was developing far from the trailing edge, which results in the formation of large separating region in the downstream as presented in Nakano et al. (2007).

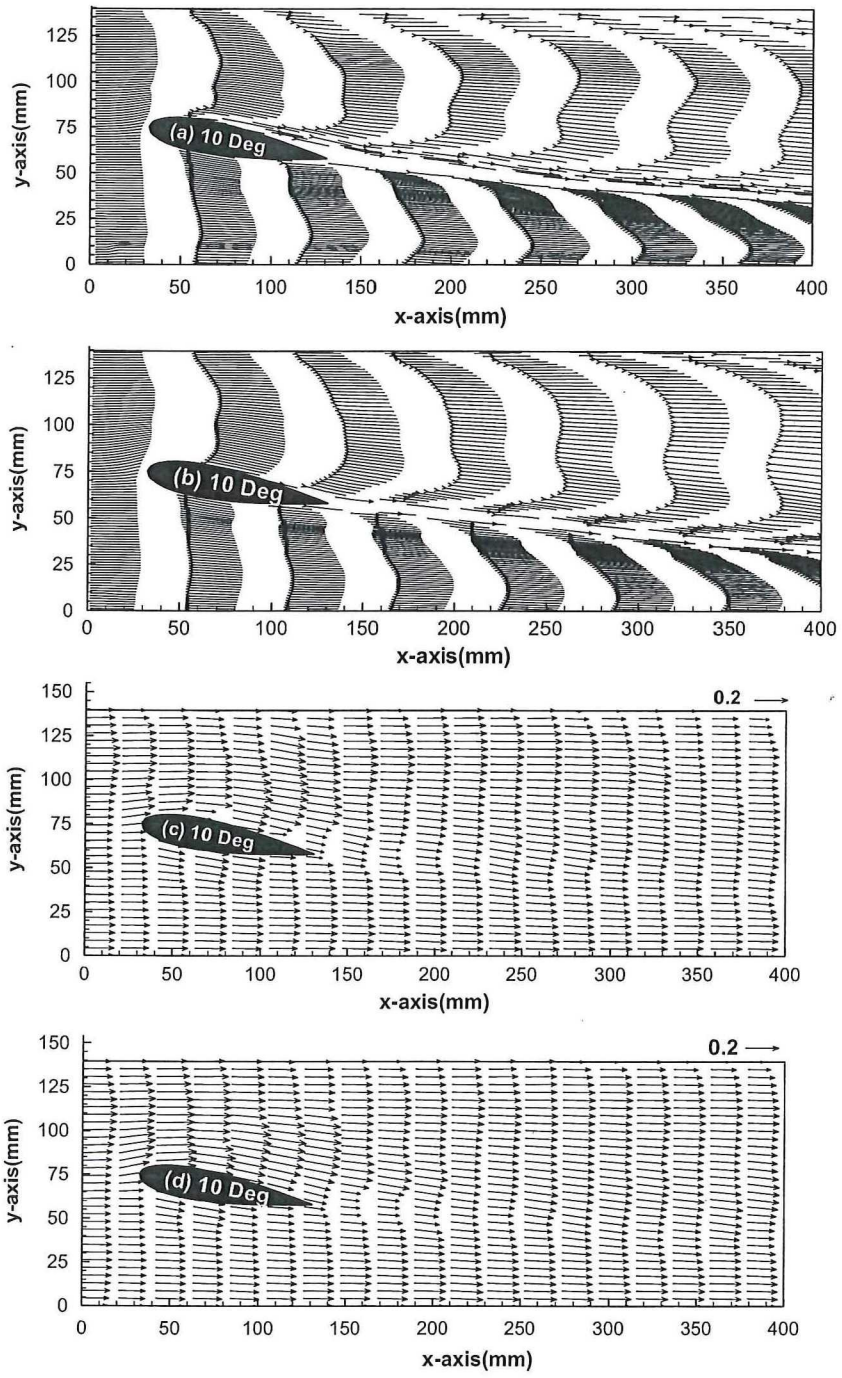

Fig. 5. Time-mean streamlines [(a) without endplate (b) with endplate] and velocity field [(c) without endplate (d) with endplate] at mid-span ($\alpha=10^{\circ}$).

There were a number of vertices in the boundary layer in Fig. 4(c) and (e). The turbulence flow after the foil oscillates upward and downward alternately. An important consequence of flow separation is the formation and shedding of circulating fluid, called vortices, in the wake region. The periodic generation of these vortices in the downstream is referred to as vortex shedding. These vortices were larger than those of the attack angles, $\alpha=15°$. As referred to Nakano et al. (2007) on the separation and reattachment of the flow around NACA 0018, the periodic vortex structure is generated over the pressure surface near the trailing edge, which is followed by the formation of periodic vortex shedding in the wake. As increased angles of attack, the flow separation point moves to the leading edge and the boundary layer keeps fully attached flow on the surface. The zero and negative values in the vector field to cause the inverse flow are found above the foil surface of Fig. 4(e) $\alpha=20°$. The backflow generates because of pressure difference due to low velocities in the wall turbulence, which increase drag force. It will form the inverse pressure gradient not to have laminar flow region. The flow formation could not maintain the thin boundary layer any more but have wake passing through the trailing edge with a thick turbulent shear layer. Figs. 5–8 show streamlines and velocity fields around NACA 0018 at attack angles $\alpha=10°$ and 20° with and without the endplate. The magnitude of mean velocity is defined by $\sqrt{\overline{u}^2+\overline{v}^2}$, where $\overline{u}$, $\overline{v}$ are the time-mean velocity magnitude in streamwise and normal direc tion respectively. The velocity gradient above the foil surface increases gradually from the leading edge to the trailing edge. The rapid velocity distribution appears above the leading edge in all cases.

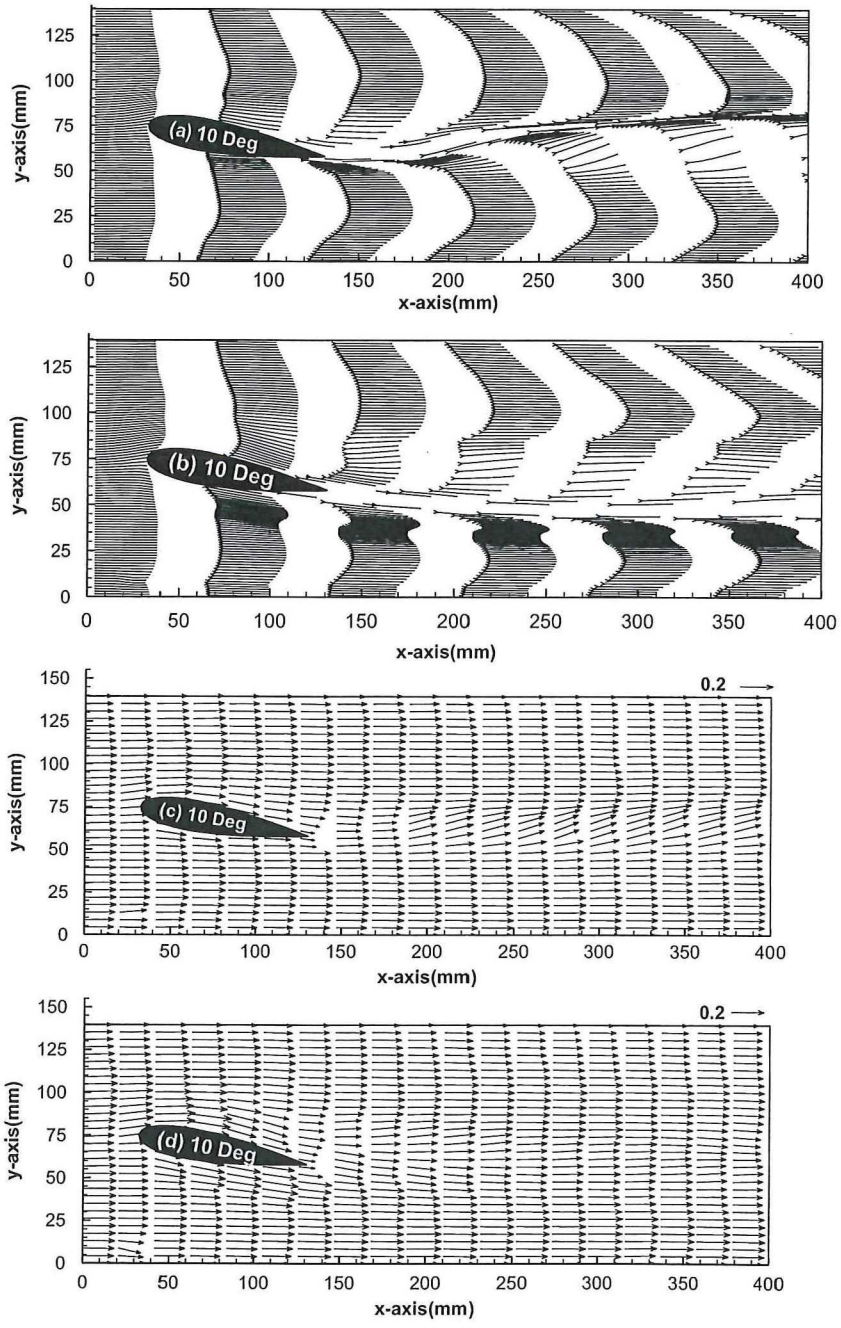

Fig. 6. Time-mean streamlines [(a) without endplate (b) with endplate] and velocity field [(c) without endplate (d) with endplate] at tip-span section ($\alpha=10°$).

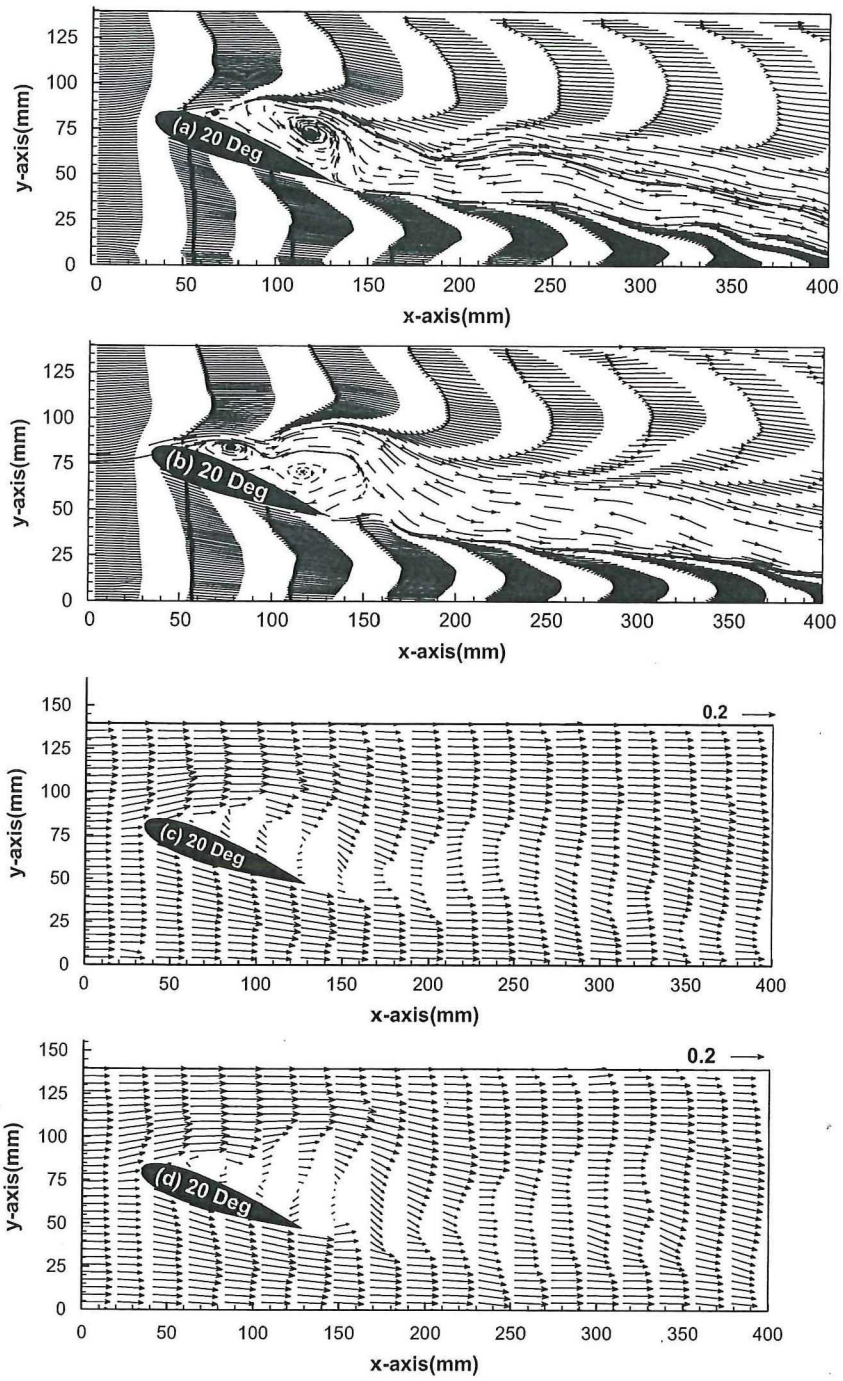

Fig. 7. Time-mean streamlines [(a) without endplate (b) with endplate] and velocity field [(c) without endplate (d) with endplate] at mid-span section ($\alpha=20^{\circ}$).

In Fig. 5 $\alpha=10^{\circ}$ at the mid-span section, the flow separation does not appear. As referred to Yao et al. (2011) on numerical simulation for NACA 0018, the flow separation did not occur around the foil under attack angles $\alpha=13^{\circ}$. In the present results, regardless whether the plate is attached or not in the mid-span at attack angles $\alpha=10^{\circ}$ in Fig. 5(a) and (b), the flow formation does not have significant effects around the foil and in the wake region. However, in the velocity field in Fig. 5(c), the velocities above the foil surface are decreased better than Fig. 5(d), which is similar with the streamlines near the foil surface in Fig. 5(a). It is expected that the influence of the endplate attached at the tip-end slightly affects this to the mid-span. The velocity field well depicts laminar flow as shown in Fig. 5(d).

Fig. 6 shows time-mean velocity field and streamlines at $\alpha=10^{\circ}$ at the tip-span section. Contrary to the flow phenomenon in Fig. 5, the flow follows the foil surface more smoothly in the latter figure. After that, it passes through the wake region, which upward wake flow occurs after the trailing edge in Fig. 6(a). According to Owen and Bryden (2005), lift-induced drag is created when there is flow around the foil tip from the high pressure side to the low pressure side. This effect is relatively simple to diminish by the use of the endplate to inhibit the vortex generation. This requires that the foil be well aligned with the free stream. Therefore, the roll-up flow in the wake region is caused by pressure difference between upper and lower foil surface as shown in Fig. 6(a). It is supposed to have vibrations and

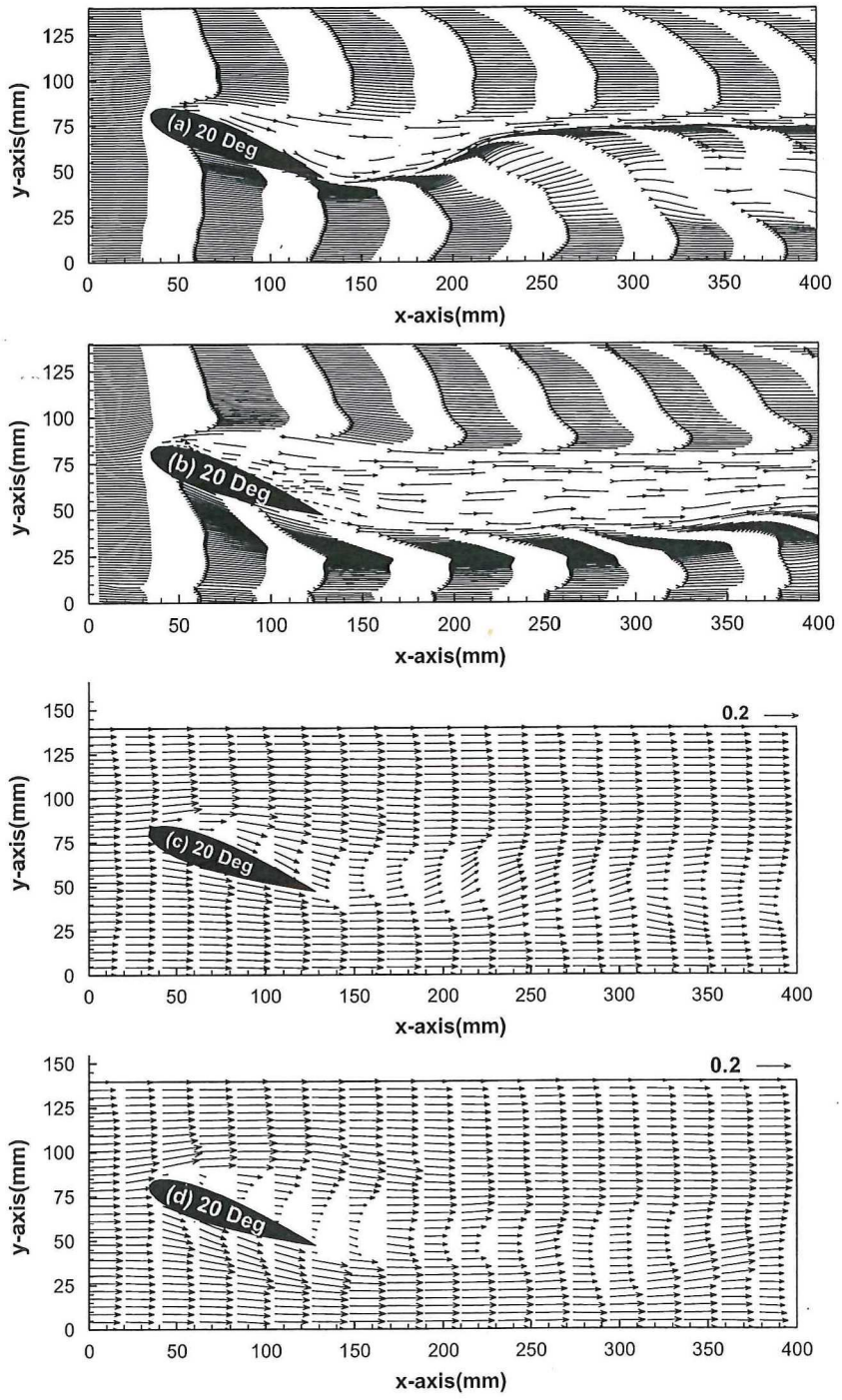

Fig. 8. Time-mean streamlines [(a) without endplate (b) with endplate] and velocity field [(c) without endplate (d) with endplate] at tip-span section (α=20°).

cavitations around the foil. The upward wake flow disappears because of the effect of the endplate in Fig. 6(b) and (d) compared with that of Fig. 6(a) and (c). The streamlines clearly illustrate that how the flow formation has created in the boundary layer.

Fig. 7 shows time-mean velocity field and streamlines around the foil at attack angle α=20° with and without the endplate at the mid-span section. The approximate location of the flow separation point can predict in Fig. 4(c), flow visualization and Fig. 7, streamlines and velocity field. The flow separation starts from the leading edge as shown in Fig. 7. Two vortices are generated on the foil surface; one small vortex appears, near the leading edge next to the separation point, and another larger one appears near the trailing edge. The flow vibrates up and down alternatively in both cases in the wake region, even if they are time-mean domain. No sign of significant effects have appeared on flow in the wake region regardless of being attached the endplate at α=20°. The occurrence of vortex shedding often causes the near-wake fluid to rapidly circulate and constantly change direction due to the alternate roll-up of the shear layer. This unsteady chaotic mixing of the fluid induces a pressure differential across the surface of the foil, which reaches a maximum at the trailing edge (Do et al., 2010). The velocity field in Fig. 7(c) and (d) tells the magnitude of the vectors and their directions. The negative and inverse directional vectors in and

around the vortex region clearly appear on the foil surface. Comparing with the both cases, with and without the endplate in the streamlines, the vortices in the case of being attached the endplate appear thinner than the others. Furthermore, the streamlines in the wake turbulence region are more stable in Fig. 7(b) compared with those in Fig. 7(a). Looking at these phenomena in terms of vibration and sound, decreasing of the vortex shedding and frequency in the wake has the effect of reducing vibration and noise (Takagi et al., 2006; Kim et al., 2006; Nakano et al., 2007).

Fig. 8 shows time-mean velocity field and streamlines around the foil at attack angle $\alpha=20^\circ$ with and without the endplate at the tip-span section. In Fig. 8(a) without the endplate at the tip-span compared with Fig. 7, two vortices have disappeared above the foil surface, and the upward wake flow dominates. The roll-up flow formation is generated in the vicinity of X=200 mm. It is expected that the outward flow from the tip-side affect the dissipation of vortices. As indicated in Fig. 4 above, this shows the dissipation of turbulence due to the pressure difference between the high pressure on the foil surface and the low pressure outside the tip-end from the span direction. The turbulent flow is decreases at tip-span because the flow outside of the tip is faster than the turbulent flow above the foil surface. In the case of being attached the endplate in Fig. 8(b), the upward wake flow disappears when compared with that in Fig. 8(a). The flow after the leading edge follows the main stream without disturbance flow except for the velocity deficiency in Fig. 8(b) and (d). The endplate makes streamwise streaks behind the foil without roll-up flow and vortices in the wake region of the tip-span side. The endplate prevented high-pressure flow escaping at the tip and causes an increase in the lift and lift-drag ratio further as presented in Park et al. (2008). They also insisted that the tip vortices are generated from the tip surface and their strength are weak and diminished rapidly.

Fig. 9 shows the profiles of time-mean velocity magnitude along the normal direction, X=75, X=150, X=250 and X=350 mm respectively, at the mid-span section. Velocity profiles indicate similar distributions in the middle of the foil in Fig. 9(a) at $\alpha=10^\circ$. In case of $\alpha=20^\circ$ at Fig. 9(a) regardless of being attached the endplate, the velocity magnitude are lower than the attack angle $\alpha=10^\circ$ in the range of Y=75–100 mm. Figs. 4–8 show this clearly in the velocity field because the vector direction is reversed when the vortices in the turbulent shear layer are generated and a new one developed. The circulation in the layer needs to be reduced to increase the lift force. In the trailing edge (X=150 mm and X=250 mm), the profiles of the velocity magnitude in case of being attached the endplate are smaller than in cases of those not attached the endplate.

Fig. 10 shows the profiles of time-mean velocity magnitude along the normal direction, X=75, X=150, X=250 and X=350 mm respectively at tip-span section. The velocity magnitude profiles in the middle of the foil (X=75 mm) and trailing edge (X=150 mm) are increased as compared with those of Fig. 9. At X=250 mm in Fig. 10(c), the whole lines into these figures appear unstable and fluctuate. The velocity magnitude distribution with the endplate indicated more stable variation from the mean value. At the profiles of X=350 mm in Fig. 10(d), the velocity magnitude distribution does not coincide with the results as generated in range of Y=0–50 mm of $\alpha=20^\circ$ in Fig. 9. The roll-up flow induced by free stream at the tip-end causes these low velocity values.

Figs. 11 and 12 show the vorticity fields around the foil at $\alpha=20^\circ$ with and without the endplate. The vorticity is equal to

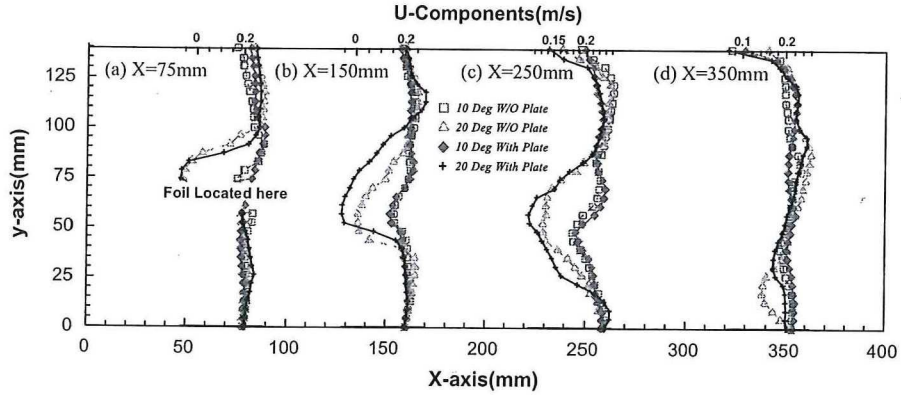

Fig. 9. Profiles of time-mean velocity magnitude at mid-span section.

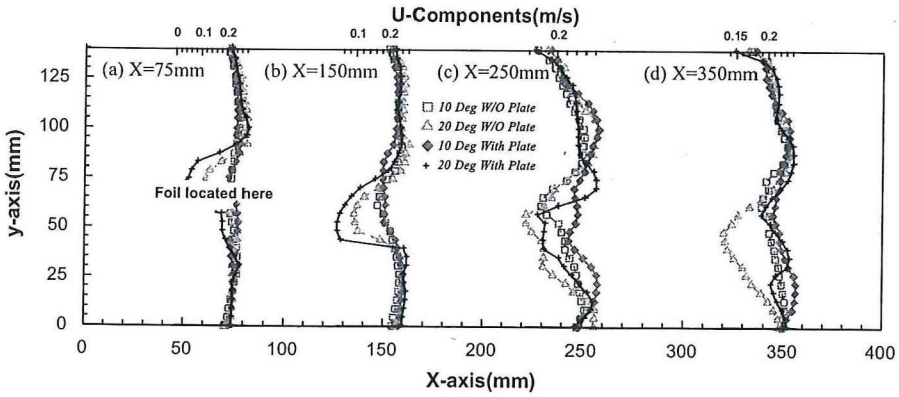

Fig. 10. Profiles of time-mean velocity magnitude at tip-span section.

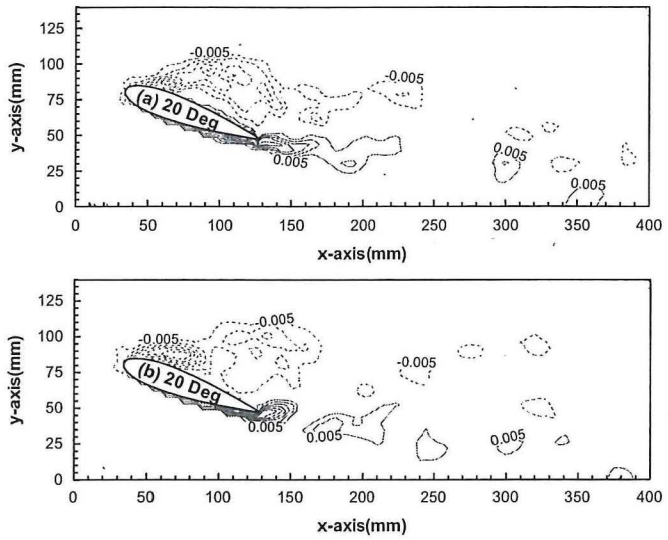

Fig. 11. Time-mean vorticity fields at mid-span section (a) without endplate (b) with endplate (α=20°) $-0.03 \le \zeta \ge 0.03$ $\Delta\zeta$=0.005 between the lines.

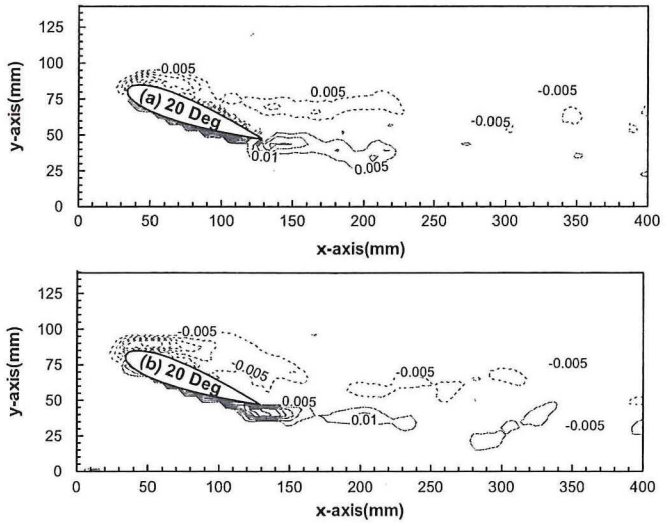

Fig. 12. Time-mean vorticity fields at tip-span section (a) without endplate (b) with endplate (α=20°) $-0.03 \le \zeta \ge 0.03$ $\Delta\zeta$=0.005 between the lines.

twice the angular velocity of a fluid particle, which is defined as:

$$\zeta = 2\varpi = \frac{\partial v}{\partial x} - \frac{\partial u}{\partial y} \tag{1}$$

where ω is angular velocity, and u and v are velocity components respectively. At the mid-span of attack angles α=20° in Fig. 11, the vorticity strength resembles each other regardless of the attachment of the endplate. The largest negative vorticity occurred in the leading edge as dotted lines, implying clockwise rotation of fluid particles in that region and the solid lines represent large positive vorticity below the foil surface. It is due to the large velocity gradient encountered in this region of the flow field; the boundary layer separates from the foil at the leading edge and forms the thin shear layer across which the velocity changes rapidly. The concentration of vorticity in the shear layer diminishes as vorticity diffuses downstream.

Fig. 12 shows time-mean vorticity fields around the tip-span of the foil at α=20°. The strong vorticity of clockwise rotation is located near the leading edge and the strong counter-clockwise rotation is generated near the trailing edge. The Reynolds shear layer of vorticity decreases compared with the vorticity in the middle of the span in Fig. 11. In Fig. 12(b) attached with the endplate at the tip-span section, the contour lines of the counter-clockwise rotation reach until the end of the flow field. This tendency is similar to the results of the vorticity field of Fig. 11 at the mid-span section. The viscous of free stream outside the foil causes the dissipation of vortices inside of the tip-span section. The similarity of vorticity field with the mid-span section occurs because the endplate attachment blocks the lateral inflow from outside the foil's tip. I envisage that the flow velocity outside of the tip is faster than inside of the tip. The vorticity decreases above the foil surface and wake region because of the lateral velocity gradients. The velocity changes rapidly in its region.

Figs. 13 and 14 show Reynolds shear stress in the wake at α=20. Reynolds shear layer fields are extracted and compared with and without the endplate at mid-span section. The time-mean Reynolds shear stress is defined as:

$$\overline{\tau_{xy}} = \frac{\rho}{T}\int_0^T u'v'dt \tag{2}$$

where u' and v' are velocity fluctuation components.

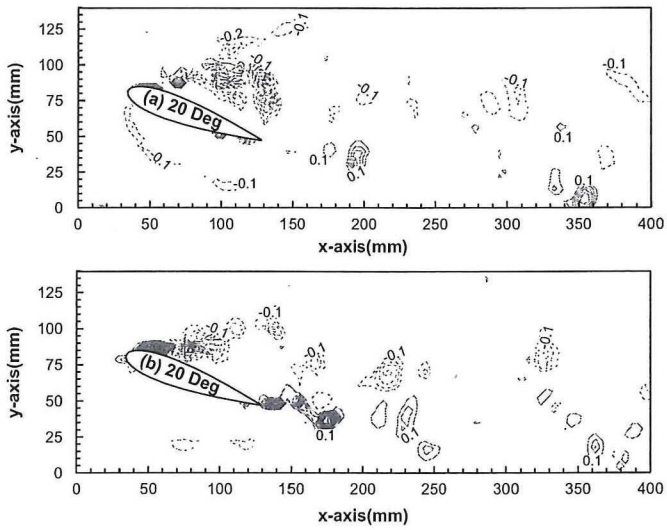

Fig. 13. Time-mean Reynolds shear stress fields at mid-span section (a) without plate (b) with plate (α=20°) $-0.5 \le \tau \ge 0.5$ $\Delta\tau$=0.1 between the lines.

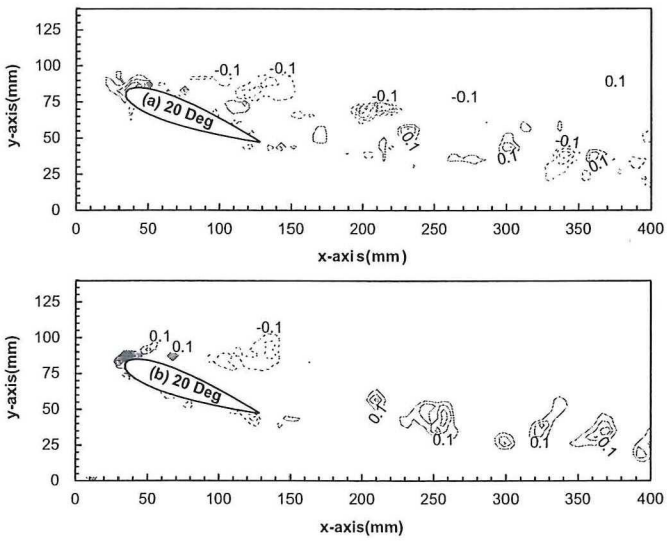

Fig. 14. Time-mean Reynolds shear stress fields at tip-span section (a) without plate (b) with plate (α=20°) $-0.5 \le \tau \ge 0.5$ $\Delta\tau$=0.1 between the lines.

Wang et al. (2009) reported that the shear layers in the upper and lower sides of the foil are shown by the concentration of positive (+) and negative (−) Reynolds shear stress. Fig. 13 shows the time-mean Reynolds shear stress in the mid-span section at $\alpha=20^{\circ}$ with and without the endplate. Reynolds shear stress in Fig. 13(a) without the endplate shows relatively low values compared to those of Fig. 13(b). The strong Reynolds shear stress is generated at the leading edge and the trailing edge, with the flow separation point as indicated in Fig. 13(b). Fig. 13(b) also shows the stronger Reynolds shear stress in the wake region after the foil as opposed to that of Fig. 13(a). It is considered that the endplate at the mid-span side increases Reynolds shear stress because the plate defends the inflow from the outside of the foil's lateral axis (Z-axis). Hence, the inflow in the mid-span area runs more freely along the foil surface under the turbulence shear layer at $\alpha=20^{\circ}$. Therefore, the strength of turbulence flow might have generated and dissipated.

Fig. 14 shows Reynolds shear stress near the end-span section at $\alpha=20^{\circ}$ with and without an endplate. Fig. 14 shows a depressed Reynolds shear stress compared to that of Fig. 13. The stronger one also dominates at the leading edge of the foil.

The positive solid lines alternates with the negative dotted lines in Fig. 14(a) without being attached the endplate in the wake region after flow separation at the leading edge. Fig. 14(b) shows Reynolds shear stress at the tip-span section with being attached the endplate. The positive contour lines are arranged in a row after the training edge. The Reynolds shear stress is curled sporadically in a streamwise direction.

Figs. 15 and 16 show cross-sectional profiles of Reynolds shear stress in the wake region with and without attachment to the endplate. Fig. 15 shows the Reynolds shear stress of cross-sectional distributions at X=250 mm of $\alpha=10$. The Reynolds shear stress of upper and lower sides at mid-span section has the same values as zero. The Reynolds shear stress sharply decreases in the range of $y=40$–90 mm especially, with no attachment to the endplate. At the end-span section, the Reynolds shear stress decreases greater than at the mid-span. Furthermore, the endplate has an outstanding effect because of converging to the Reynolds shear stress.

Fig. 16 shows the cross-sectional profiles of Reynolds shear stress at X=350 mm of $\alpha=20$. At the mid-span of the foil, the high negative values appear in the middle of the Y-axis. Nevertheless, the values of Reynolds shear stress in the case of being attached the endplate are distributed at almost zero. The low

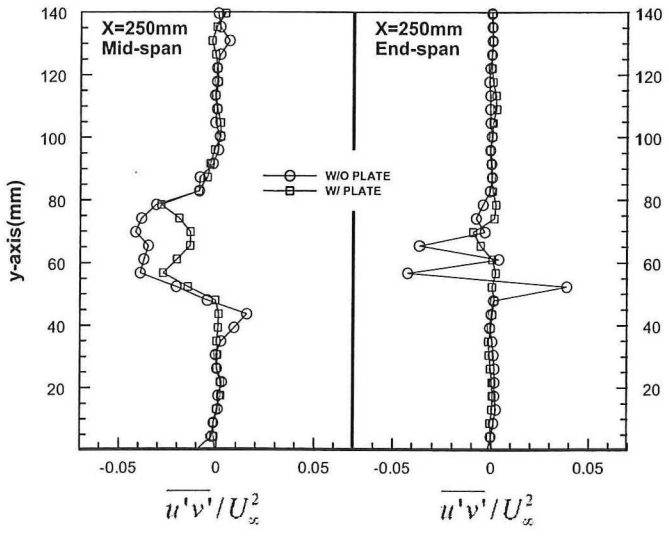

Fig. 15. Cross-sectional profiles of Reynolds shear stress at 10°.

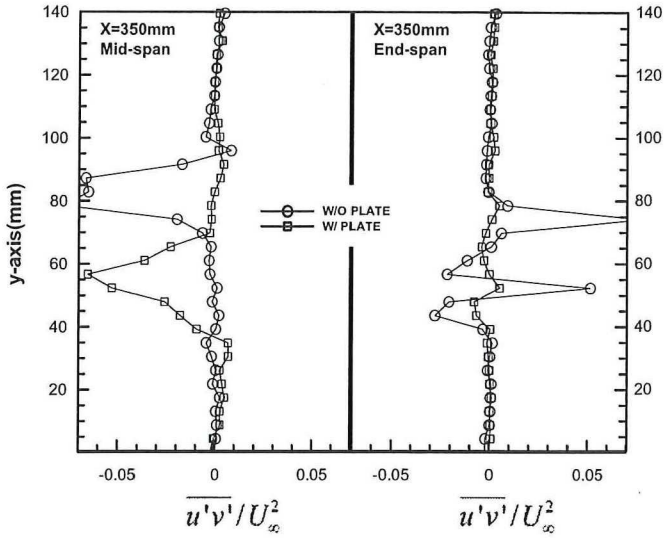

Fig. 16. Cross-sectional profiles of Reynolds shear stress at 20°.

Reynolds shear stress results are scattered in the wide range of the Y-axis greater than the end-span sectional distributions. At the end-span section, the lower negative values have almost disappeared. The high Reynolds shear stress is appeared in the bare foil. However, Reynolds shear stress is also concentrated at zero values in the case of being attached the endplate. This means that the plate attached at the end of the foil has an outstanding effect on stabilizing the Reynolds shear stress in the wake region.

4. Conclusions

This article considered here the flow patterns and profiles around NACA 0018 foil at $Re=2.5\times10^4$ to verify the effect of an end plate being attached at the end-span. The flow around the foil with a variety of attack angles with and without the endplate were visualized and measured flow fields using a 2-frame cross correlation PIV method. The following results are summarized based on our observations and data analysis.

1. PIV system proves itself useful in demonstrating the flow characteristics around a foil while being attached an endplate and can obtain typical vortex formation as well as velocity information in the vicinity of the foil. The endplate gives outstanding effects in securing a stable hydrodynamic performance, especially on the tip-span side. Almost all vessels could greatly benefit from the use of the high-lift foil for their various purposes.
2. The endplate significantly stabilizes the Reynolds shear stress and reduces the tip vortex, causing the prevention of vibration and cavitations. The roll-up wake flow at the span-end of the foil decreased due to the endplate. The Reynolds shear stress decreased at $\alpha=10^{\circ}$ and $\alpha=20^{\circ}$ in the wake region.
3. The endplate makes streamwise streaks behind the foil without roll-up flow and vortices in the wake region of the tip-span side. The strong vorticity of clockwise rotation appears near the leading edge and a strong counter-clockwise rotation is generated near the trailing edge. The vortices decrease above the foil surface and wake region because of the lateral velocity gradients.
4. The total side forces of a foil concerned with complex lift and drag forces should be considered, as well as the interaction with hull, propellers and rudders behind a ship. This also should be applied to blades to generate wind and current

energy and for fin stabilizers to control the streamwise and normal directional fluid motion.

References

Ahn, H.S., Kim, H.C., 2003. An experimental study of coanda effect on the flapped control surfaces. J. Soc. Naval Architects Korea 40 (5), 10–16.

Carter, A.W., 1961. Effect of ground proximity on the aerodynamic characteristics of aspect-ratio-1 airfoils with and without end plate. NASA Tech. Note 926, 1–9.

Cory, S.J., James, C.R., Russell, M.C., 1998. Numerical investigation of an airfoil with a Gurney flap. J. Aircraft Des. 1, 75–88.

Daichin, K.W., Zhao, L.L., 2007. PIV measurements of the near-wake flow of an airfoil above a free surface. J. Hydrodyn. 19 (4), 482–487.

Do, T., Chen, L., Tu, J., 2010. Numerical study of turbulent trailing-edge flows with base cavity effects using URANS. J. Fluids Struct. 26, 1155–1173.

Farsimadan, E., Dehghan, M.R., 2010. An experimental study of the turbulence quantities in the boundary layer and near-wake of an airfoil placed at upstream of a 90 bend. Exp. Therm. Fluid Sci. 34, 979–991.

Grant, I., McCutcheon, G., McColgan, A.H., Hurst, D., 2006. Optical-velocimetry, wake measurements of lift and induced drag on a wing. J. Opt. Lasers Eng. 44, 282–303.

Kim, H.J., Lee, S., Fujisawa, N., 2006. Computation of unsteady flow and aerodynamic noise of NACA 0018 airfoil using large-eddy simulation. Int. J. Heat Fluid Flow 27, 229–242.

Kobayashi, H., Ishbashi, A., 1993. A study on the interaction among the Hull, Propeller and Rudder for the ship with twin-propeller twin rudder. J. Jpn. Inst. Navig. 87, 171–179.

Lam, W., Hamil, G.A., Song, Y.C., Robinson, D.J., Raghunathan, S., 2011. A review of equations used to predict the velocity distribution within a ship's propeller jet. Ocean Eng. 38, 1–10.

Lee, Y.G., Yu, J.W., Kang, B.H., Pak, K.R., 2008. A numerical study on the flow around a rudder behind low speed full ship. J. Ship Ocean Tech. 12 (2), 41–52.

Nakano, T., Fujisawa, N., Oguma, Y., Takagi, Y., Lee, S., 2007. Experimental study on flow and noise characteristics of NACA 0018 airfoil. J. Wind Eng. 95, 511–531.

Owen, A., Bryden, I.G., 2005. Prototype support structure for seabed mounted tidal current turbines. J. Eng. Maritime Environ. 219, 173–183.

Paik, B.K., Kim, K.Y., Kim, K.S., Park, S.H., Heo, J.K., Yu, B.S., 2010. Influence of propeller wake sheet on rudder gap flow and cap cavitation. Ocean Eng. 36 (16), 1418–1427.

Park, K.W., Hong, C.H., Kim, K.S., Lee, J.H., 2008. Effect of endplate shape on performance and stability of wing-in ground (WIG) craft. World Acad. Sci. Eng. Tech. 47, 296–302.

Park, K.W., Lee, J.H., 2008. Influence of endplate on aerodynamic characteristics of low-aspect-ratio wing in ground effect. J. Mech. Sci. Tech. 22, 2578–2589.

Pass, H.R., 1940. Analysis of wind-tunnel data on directional stability and control. Nat. Advisory Committee Aeronau. NACA Tech. Note 755, 1–5.

Seo, D.W., Jeong, S.W., Lee, S.H., 2007. Influence of tail blades on the performance of a fin. J. Soc. Naval Architects Korea 44 (2), 55–63.

Tang, D., Dowell, E.H., 2006. Aerodynamic flow control of an airfoil with small trailing edge strips. J. Aircraft 43 (6), 1854–1866.

Takagi, Y., Fujisawa, N., Nakano, T., Nashimoto, A., 2006. Cylinder wake influence on the tonal noise and aerodynamic characteristics of a NACA 0018 airfoil. J. Sound Vibr. 297, 563–577.

Wang, F., Jin, F., Qi, Z., 2009. Modeling for active fin stabilizers at zero speed. J. Ocean Eng. 36, 1425–1437.

Weier, T., Gerbeth, G., 2004. Control of separated flows by time periodic Lorentz forces. Eur. J. Mech. 23, 835–849.

Yao, J., Yuan, W., Wang, J., Xie, J., Zhou, H., Peng, M., Sun, Y., 2011. Numerical simulation of aerodynamic performance for two dimensional wind turbine airfoils. Proc. Procedia Eng. 31, 80–86.

Yu, L., Lashimi, N., Robert, J.E., Krishan, K.A., Gaeta, R., 2005. Computational evaluation of the steady and pulsed jet effect on the performance of a circulation control wing section. The Am. Inst. Aeronaut. Astronaut. 5, 295–321.